

# Optimization of a Two-Fluid Hydrodynamic Model of Churn-Turbulent Flows

ICONE 17

Donna Post Guillen  
Jonathan K. Shelley  
Steven P. Antal  
Elena A. Tselishcheva  
Michael Z. Podowski  
Dirk Lucas  
Matthias Beyer

July 2009

The INL is a  
U.S. Department of Energy  
National Laboratory  
operated by  
Battelle Energy Alliance



This is a preprint of a paper intended for publication in a journal or proceedings. Since changes may be made before publication, this preprint should not be cited or reproduced without permission of the author. This document was prepared as an account of work sponsored by an agency of the United States Government. Neither the United States Government nor any agency thereof, or any of their employees, makes any warranty, expressed or implied, or assumes any legal liability or responsibility for any third party's use, or the results of such use, of any information, apparatus, product or process disclosed in this report, or represents that its use by such third party would not infringe privately owned rights. The views expressed in this paper are not necessarily those of the United States Government or the sponsoring agency.

## OPTIMIZATION OF A TWO-FLUID HYDRODYNAMIC MODEL OF CHURN-TURBULENT FLOWS

**Donna Post Guillen\***  
**Jonathan K. Shelley**

Advanced Process and Decision  
Systems Department, Idaho National  
Laboratory, Idaho Falls, ID 83415,  
USA

[\\*Donna.Guillen@inl.gov](mailto:Donna.Guillen@inl.gov)

**Steven P. Antal**  
**Elena A. Tselishcheva**  
**Michael Z. Podowski**

Center for Multiphase Research,  
Rensselaer Polytechnic Institute,  
Troy, NY 12180, USA

**Dirk Lucas**  
**Matthias Beyer**

Institute of Safety Research,  
Forschungszentrum Dresden-  
Rossendorf,  
Dresden, Germany

### KEY WORDS

CFD validation, churn turbulent flow, two-fluid model, design optimization, NPHASE-CMFD, multiphase flow

### ABSTRACT

A hydrodynamic model of two-phase, churn-turbulent flows is being developed using the computational multiphase fluid dynamics (CMFD) code, NPHASE-CMFD. The numerical solutions obtained by this model are compared with experimental data obtained at the TOPFLOW facility of the Institute of Safety Research at the Forschungszentrum Dresden-Rossendorf. The TOPFLOW data is a high quality experimental database of upward, co-current air-water flows in a vertical pipe suitable for validation of computational fluid dynamics (CFD) codes. A five-field CMFD model was developed for the continuous liquid phase and four bubble size groups using mechanistic closure models for the ensemble-averaged Navier-Stokes equations. Mechanistic models for the drag and non-drag interfacial forces are implemented to include the governing physics to describe the hydrodynamic forces controlling the gas distribution. The closure models provide the functional form of the interfacial forces, with user defined coefficients to adjust the force magnitude. An optimization strategy was devised for these coefficients using commercial design optimization software. This paper demonstrates an approach to optimizing CMFD model parameters using a design optimization approach. Computed radial void fraction profiles predicted by the NPHASE-CMFD code are compared to experimental data for four bubble size groups.

### 1. INTRODUCTION

Churn-turbulent flows are often employed in industrial processes, including nuclear and chemical reactors. Numerical simulations can be used to increase our understanding of these heterogeneous flows and assist with design, operation and troubleshooting of these systems. A hydrodynamic model of two-phase, churn-turbulent flows is being developed using the computational multiphase fluid dynamics (CMFD) code, NPHASE-CMFD[1]. Traditionally, empirical correlations are used to describe two-phase flow behavior, which consequently are of limited use for system scale-up or design beyond the envelope of experimentally tested conditions and configurations. The objective of this work is to produce accurate predictions of churn-turbulent flow through development and validation of mechanistically-based models of the dominant interfacial forces. Computational simulations of two-phase, upwards air-water flow in a vertical pipe are compared to high-quality experimental data from the Transient two Phase FLOW test facility (TOPFLOW) at the Institute of Safety Research at the Forschungszentrum Dresden-Rossendorf [2].

The computational platform for this work is the NPHASE-CMFD computer program, an unstructured, finite-volume, multifield, pressure-based CMFD computer code offering both segregated and fully coupled multifield numerical solution methods. To achieve numerical convergence for multiphase flows, simulations are performed using the robust, coupled algorithm, which solves for the phasic velocity, pressure, and

volume fraction simultaneously. Although, the computer memory requirements are increased, this ability to couple the conservation of mass and momentum equations is more robust than the use of a segregated solver. A full three-dimensional, Eulerian-Eulerian framework is employed, rather than tracking a very large number of individual bubble trajectories.

Ensemble-averaged conservation equations for mass and momentum can be solved for an arbitrary number of fields or phases. The equations are discretized into a block matrix system, which is solved by an algebraic multigrid solver. A detailed derivation of the ensemble-averaged conservation equations has been given by Drew and Passman [3]. The fully coupled mass/momentum scheme allows any field/phase to interact with any other field/phase via mass, momentum and/or energy transfer. Interfacial mass, momentum and turbulence sub-models provide coupling between the fields and phases. Turbulence in the bulk fluid was modeled using a standard k- $\epsilon$  model with the two-phase turbulence viscosity given by Sato [4, 5].

## 2. CMFD MODEL FORMULATION

A five-field, ensemble-averaged CMFD model was created to simulate two-phase, churn-turbulent flows in a vertical pipe. A more comprehensive description of the governing equations is given in a companion paper [6] and therefore will not be repeated here.

Flow structure visualization studies [7] show a clear separation of bubble sizes for churn turbulent flows. The TOPFLOW experimental data reveals a broad spectrum of bubble sizes for the churn-turbulent flow regime. Small bubbles (from 2 to 6 mm) are spherical to ellipsoidal in shape, whereas the larger bubbles ( $\geq 10$  mm) vary in size with gas flow and exhibit a distorted, spherical cap shape. The churn-turbulent flow is modeled as a continuous liquid phase with four dispersed bubble size groups. Each bubble group is treated as a separate field to allow appropriate flow physics for the different bubble size groups to be included via the closure models. The use of different closure models for bubble forces is discussed by [8, 9].

### 2.1 Development of Mechanistic Models for Interfacial Forces

A key factor for properly modeling the hydrodynamics of two-phase flows is the formulation of consistent mechanistic closure laws that describe the dominant mass and momentum interactions at the fluid interfaces. Closure relations are needed to reintroduce the information that was lost as a result of averaging the conservation equations. These closure laws account for the sub-scale mass and momentum transfer between the various fields and phases. The closure models provide the functional form expected for the interfacial forces. However, local condition dependent coefficients are expected since the closure models are derived for ideal bubbly flow conditions and applied to churn-turbulent flows. The flow is assumed to be adiabatic and only the momentum exchange at the bubble interface is considered. The ensemble-averaged, phasic momentum conservation equation can be reduced to the following approximate multifield formulation for field-k [10]

$$\frac{\partial}{\partial t} (\alpha_k \rho_k \underline{v}_k) + \nabla \cdot (\alpha_k \rho_k \underline{v}_k \underline{v}_k) = -\alpha_k \nabla p + \alpha_k \nabla \cdot \underline{\tau}_k + \alpha_k \rho_k \underline{g} + \underline{M}_k^i \quad (1)$$

The terms on the right hand side of Equation 1 represent the pressure gradient, shear stress tensor, body force due to gravity and momentum exchange at interfaces. Mass transfer due to bubble breakup and coalescence is not considered here. In our model, field 1 represents the continuous liquid phase and fields 2 through 5 represent the dispersed bubble groups.

The compatibility condition included in the coupled solver equation set is expressed as

$$\sum_{k=1}^5 \alpha_k = 1 \quad (2)$$

The sum of forces on the dispersed bubble fields is equal and opposite to that on the continuous liquid field.

$$\underline{M}_{c,k}^i = -\underline{M}_{d,k}^i \quad (3)$$

The interfacial interactions between the individual bubble fields are specified by mechanistic models for both drag and non-drag forces. The interfacial momentum transfer force,  $\underline{M}_{d,k}^i$ , is partitioned into drag and nondrag components

$$\underline{M}_{d,k}^i = \underline{M}_{d,k}^D + \underline{M}_{d,k}^{ND} \quad (4)$$

where

$$\underline{M}_{d,k}^{ND} = \underline{M}_{d,k}^L + \underline{M}_{d,k}^W + \underline{M}_{d,k}^{TD} + \underline{M}_{d,k}^{VM} \quad (5)$$

The interfacial momentum transfers considered important for churn-turbulent flow in a bubble column include the interfacial drag force as well as interfacial non-drag forces consisting of the lift force, the wall force, the turbulence dispersion force and the virtual mass force. Other forces, such as the Basset force, may also be present but are small and therefore neglected here.

The interfacial drag force is written as

$$\underline{M}_{d,k}^D = -\frac{1}{8} C_{D,k} \rho_c |\underline{v}_{d,k} - \underline{v}_c| (\underline{v}_{d,k} - \underline{v}_c) A_{i,k}'' \frac{r_{sm,k}}{r_d} \quad (6)$$

where the subscript c denotes the continuous field/phase and d denotes the dispersed field/phase (i.e., the bubbles). The ensemble-averaged fluid velocity of field-k is  $\underline{v}_k$ , the local volume fraction is  $\alpha_k$ , and the density is  $\rho_k$ . The interfacial area density  $A_{i,k}''$  is modeled assuming a spherical dispersed phase as

$$A_{i,k}'' = f_k \frac{6\alpha_k}{D_k} \quad (7)$$

The interfacial area density can be modified by a shape factor,  $f_k$ , to account for the nonspherical shape of the bubbles [11]. In Equation 6, the Sauter mean radius is given as

$$r_{sm,k} = \frac{3\forall_k}{A_{ik}''} \quad (8)$$

and the drag radius is expressed as

$$r_{d,k} = \frac{3\forall_k}{4A_k}. \quad (9)$$

In these equations,  $\forall_k$  and  $A_k$  are the bubble volume and projected area, respectively. The term  $\frac{r_{sm,k}}{r_d}$  is 1.0 for small bubbles, whereas for large bubbles it is approximately 1.8. For the large cap bubbles, the surface area of a partial sphere is projected assuming a wake angle of  $50^\circ$  (see [12]). The drag coefficient  $C_{D,k}$  for the small bubbles is expressed as [13]

$$C_{D,k} = \frac{24}{Re_k} \left( 1 + 0.1 Re_k^{0.75} \right) \quad (10)$$

where

$$Re_k = \frac{D_k \rho_c (\underline{v}_{d,k} - \underline{v}_c)}{\mu_m} \quad (11)$$

with a mixture viscosity defined as

$$\mu_m = \frac{\mu_c}{1 - \alpha_d} \quad (12)$$

where

$$\alpha_d = \sum_{k=2}^5 \alpha_k \quad (13)$$

The drag coefficient  $C_D$  for the large cap bubbles is given as [14]

$$C_{D,k} = \frac{8}{3} (1 - \alpha_k)^2 \quad (14)$$

For simplicity, the bubbles are considered to be rigid spheres, although it is known that internal circulation within the bubbles can decrease the drag [15].

The effective dispersed phase diameter  $D_k$  and the drag coefficient  $C_{D,k}$  are input by the user. The drag forces on the bubbles oppose the direction of liquid flow. The forces acting in the axial direction include drag, gravity and buoyancy.

The criterion used with the drag coefficient for classifying bubble size as either small or large is based bubble chord length given by [14] as

$$D_{cr} = 4 \sqrt{\frac{\sigma}{g(\rho_c - \rho_d)}} \quad (15)$$

which is approximately 10.8 mm for air-water flow at the TOPFLOW conditions [7]. Bubbles smaller than this size tend to be spherical or ellipsoidal in shape, whereas those larger than this size exhibit a distorted, spherical cap shape.

The interfacial lift force accounts for the lateral forces between the dispersed and continuous phase due to aerodynamic lift and is expressed as

$$\underline{M}_{d,k}^L = -C_{L,k} \rho_c \alpha_k (\underline{v}_{d,k} - \underline{v}_c) \times (\nabla \times \underline{v}_c) \quad (16)$$

The approach for determining the lift force is similar to that employed by [8]. The lift force coefficient is based upon the correlation for poly-dispersed flows given by [16]

$$C_{L,k} = \begin{cases} \min(0.288 \tanh(0.121 Re_k), f(Eo_k)) & Eo_k < 4 \\ f(Eo_k) & 4 < Eo_k < 10 \\ -0.27 & Eo_k > 10 \end{cases} \quad (17)$$

with

$$f(Eo_k) = 0.00105 Eo_k^3 - 0.0159 Eo_k^2 - 0.0204 Eo_k + 0.474 \quad (18)$$

where  $Eo_k$  is the Eötvös number calculated as

$$Eo_k = \frac{g(\rho_c - \rho_d) D_{h,k}^2}{\sigma}. \quad (19)$$

An empirical correlation [17] for aspect ratio of an elliptical shape bubble is used to calculate the maximum horizontal dimension of the bubble,  $D_{h,k}$

$$D_{h,k} = D_k \sqrt[3]{1 + 0.163 Eo_k^{0.757}} \quad (20)$$

since the maximum vertical dimension of the bubble is expressed as [9]

$$D_{v,k} = \frac{D_k^3}{D_{h,k}^2} \quad (21)$$

The Eötvös number is proportional to the buoyancy force divided by the surface tension force and, together with the Morton number and Reynolds number, can be used to characterize the shape of bubbles moving in a surrounding fluid. Such flow regime maps are given by Clift et al. [15].

The lift force acts on the bubbles in a direction perpendicular to the bulk flow when gradients of liquid velocity are present. It acts in a similar manner to that of an asymmetric airfoil in a uniform flow, but rather is a result of a non-uniform velocity field moving over a symmetric bubble. The effect is to move the bubbles towards or away from the pipe wall. The critical bubble diameter [18] at which the lift force changes sign can be found by solving for the roots of Equation 18. A critical Eötvös number of 6.06 is obtained, which yields a critical horizontal diameter of 6.7 mm and a critical spherical diameter of 5.8 mm. According to the Tomiyama correlation, bubbles with a diameter smaller than the critical diameter are

given a positive lift force coefficient, whereas bubbles with a diameter larger than the critical diameter are given a negative lift force coefficient. The negative lift force coefficient causes the large bubbles to migrate towards the center of the pipe for the case of co-current upward vertical pipe flow. Conversely, the smaller bubbles tend to move towards the wall. Note that if the flow direction was reversed (i.e., co-current downward flow), the behavior would be opposite.

The interfacial wall force accounts for the hydrodynamic force on a bubble traveling in close proximity to a solid wall and is expressed as

$$\underline{M}_{d,k}^w = -C_{w,k} F(\xi) \frac{2\alpha_k \rho_c |\underline{v}_{d,k} - \underline{v}_c|^2}{D_k} \underline{n} \quad (22)$$

where

$$\xi = \frac{2s}{c_\xi D_k} \quad (23)$$

In Equations 22 and 23,  $s$  is the distance between the bubble and the wall and  $\underline{n}$  is the outward normal vector at the surface of the wall. Due to the non-uniform drainage of the liquid around the bubble, a lateral lubrication-like force caused by surface tension pushes the bubbles away from the wall. The multiphase wall force only acts in a localized region adjacent to the pipe wall. The term  $c_\xi$  adjusts this region of influence and was set to 0.7. The wall force distance function  $F(\xi)$  is given as [19]

$$F(\xi) = \begin{cases} 1 + \left(\frac{\xi}{2}\right)^2 (\xi - 3) & \text{for } s < D_k \\ 0.0 & \text{for } s \geq D_k \end{cases} \quad (24)$$

The effect of the wall force is seen as a sharp spike in bubble void fraction near the wall that affects the small bubbles.

To account for the increased mixing due to turbulence in a two-phase flow, a turbulence volume fraction dispersion force is included

$$\underline{M}_{d,k}^{TD} = -C_{TD,k} \rho_c k \nabla \alpha_k \quad (25)$$

In this model, the turbulent dispersion force serves to transport the gaseous phase in a direction opposing the void fraction gradient. For isotropic turbulence, the turbulent dispersion coefficient ( $C_{TD}$ ) is assigned a value of  $\frac{2}{3}$ . Accounting for the effect of anisotropy (due to higher velocity fluctuations in the axial than in the radial direction) lowers the turbulent dispersion coefficient to  $\frac{1}{2}$  [10]. The forces acting in the radial direction include lift, wall and turbulent dispersion forces.

The virtual mass force accelerates the flow around a bubble as it accelerates through the liquid and is given by

$$\underline{M}_{d,k}^{VM} = -C_{VM,k} \rho_c \alpha_k \left\{ \left[ \frac{\partial \underline{v}_{d,k}}{\partial t} + (\underline{v}_{d,k} \cdot \nabla) \underline{v}_{d,k} \right] - \left[ \frac{\partial \underline{v}_c}{\partial t} + (\underline{v}_c \cdot \nabla) \underline{v}_c \right] \right\} \quad (26)$$

The virtual mass coefficient  $C_{VM,k}$  is specified by the user. Since our simulation is run to nearly fully developed conditions, this term does not affect the overall gas profile. The virtual mass force applied in the simulation is very small and serves only to stabilize the numerical solution by limiting the change in gas velocity between iterations.

## 2.2 Model Setup

Two cases from the TOPFLOW experiment database were selected for the optimization study [2]. Cases 118 and 140 were used since the two-phase flow is in the churn-turbulent flow regime. The bulk liquid mass flow rate is 30.336 kg/s for both cases with an inlet liquid superficial velocity of 1.017 m/s. The two TOPFLOW cases modeled were identical except for the inlet gas velocity. The inlet superficial gas velocities  $j_g$  for Cases 118 and 140 are 0.22 m/s and 0.53 m/s, respectively. A constant gas density was assigned corresponding to an outlet pressure of 176.7 kPa and 188.5 kPa for Cases 118 and 140, respectively. Future simulations will take into the account the variation in gas density over the height of the pipe.

Details regarding the experiment configuration and methodology are given in [2]. The TOPFLOW data is arranged into four bubble size groups: less than 5.8 mm, 5.8 to 7.0 mm, 7.0 to 10.0 mm, and larger than 10 mm. The smallest size bubble that can be measured by the wire mesh sensor in the TOPFLOW experiments is approximately 2 mm. The largest bubble size is constrained by the pipe inner diameter.

Table 1 shows the inlet void fraction, inlet velocity and mean bubble size specified for the five fields in the simulations. The mean bubble size corresponds to the TOPFLOW bubble size groups. For simplicity, a uniform inlet velocity and void fraction distribution were applied at the inlet. This assumption does not affect the nearly fully developed flow profiles at the exit of the test section.

The simulation replicated the experimental conditions for air-water flow in a vertical pipe with an inside diameter of 195.3 mm. An axisymmetric  $40 \times 500$  grid with refined cell size of 0.5 mm near the wall was used to represent the  $0.09765 \text{ m} \times 9.66 \text{ m}$  domain. There are 40 nodes along the radial axis and 500 axial nodes. Taking advantage of symmetry, half of the pipe was modeled. At the wall boundary, the no slip condition was invoked. A symmetry boundary condition was employed along the pipe centerline. The inlet was modeled as a velocity inlet and at the pipe exit a constant pressure boundary condition was applied. Gridgen meshing software by Pointwise, Inc. was used to create the meshes and specify boundary conditions. The mesh spacing is finer near the inlet to capture the developing flow. A grid study was performed to verify that the results obtained are grid independent.



**TABLE 1. INLET VOID FRACTION, INLET VELOCITY AND BUBBLE SIZE SPECIFIED IN SIMULATIONS.**

Field $k$	$D_k$ (mm)	Case 118		Case 140	
		$j_l = 1.017 \text{ m/s}, j_g = 0.22 \text{ m/s}$		$j_l = 1.017 \text{ m/s}, j_g = 0.53 \text{ m/s}$	
		$\alpha$ (%)	$v$ (m/s)	$\alpha$ (%)	$v$ (m/s)
1	N/A	76.0	1.32	58.2	1.681
2	3.9	3.8	1.3	2.5	1.68
3	6.4	2.5	1.3	2.0	1.68
4	8.5	5.8	1.3	6.1	1.68
5	15.	11.9	1.3	31.2	1.68

For this analysis, the convergence criteria are based upon an average root-mean-square (RMS) change in velocity, pressure and volume fraction between iterations being less than a specified tolerance. The RMS change in velocity was less than  $1.0 \times 10^{-4}$  while the pressure RMS change was less than  $1.0 \times 10^{-2}$ . These levels are low enough that further reducing the error does not change the predicted hydrodynamic profiles.

### 3. VALIDATION APPROACH

A commercial software package (Engineous iSIGHT-FD) was used to conduct a sensitivity study by varying the ranges of the closure model coefficients over their expected range. The coefficients are varied within these limits to determine the set that most closely matches experimental data. To validate the model to the experimental results, statistical methods and optimization techniques were employed to determine the family of coefficient sets that most closely match the experimental data. For this study a Latin Hypercube Sample (LHS) with the sixteen coefficients were used to generate the initial 256 runs.

Results from the computational simulations performed in a companion paper [6] were taken into consideration for the optimization study. Figure 1 outlines the validation methodology using the design optimization process. The coefficient terms in the mechanistic models described in the previous section were optimized using the experimental radial void fraction distribution measurements. This technique in effect varied the force coefficients for the drag, lift and wall interfacial forces between specified upper and lower bounds by adjusting a user multiplier. These bounds were estimated using the equations outlined in the previous subsection. The lift force coefficient calculated from the Tomiyama correlation (Equation 17) ranges between 0.288 for the smallest bubbles to -0.27 for the largest bubbles. The upper bound is well below the theoretically-derived value of 0.5 for a single bubble in potential flow.

The lift force coefficient multiplier was varied between -1.0 and 1.0. The wall force coefficient multiplier was varied between 0 and 1.0 for all bubble fields. Since the virtual mass

force is only used to stabilize the numerical solution, the virtual mass coefficient multiplier was not varied, but rather assigned a constant value of 1.0. The turbulence dispersion coefficient multiplier was varied between 0.5 and 2.0. The three forces between the four bubble size groups (Fields 2-5) and the continuous phase (Field 1) yielded a total of twelve coefficients for the optimization study.

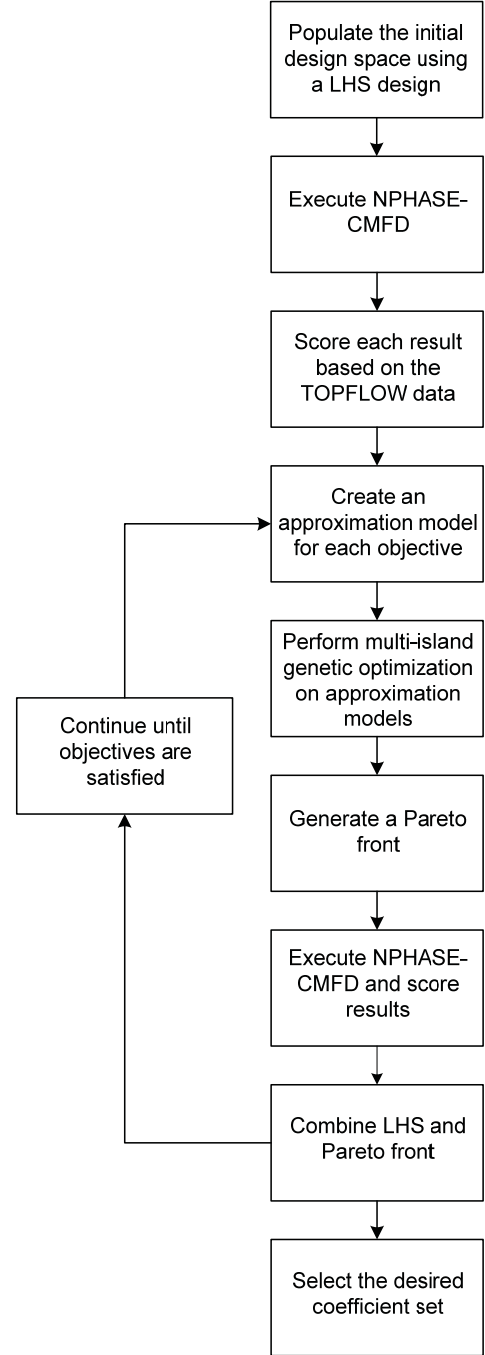


**FIGURE 1. VALIDATION METHODOLOGY USING DESIGN OPTIMIZATION PROCESS.**

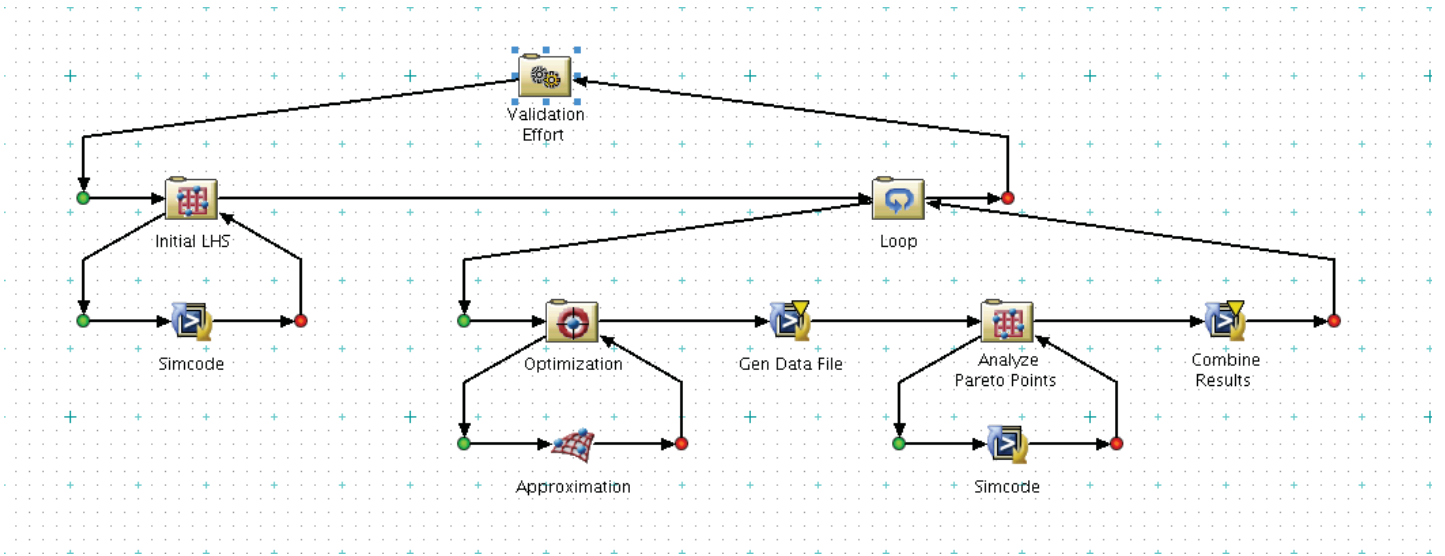


**FIGURE 2. DESIGN OPTIMIZATION PROCESS**

Four analysis functions were used for the study. Their values were obtained by using the four different nearly fully developed void fraction profiles for the experimental and simulated results and calculating the RMS values for each profile. Next, Radial Basis Functions (RBF) were created for each of the four different bubble size groups and the overall void fraction. Using the RBF models, the iSIGHT-FD genetic algorithm was used to explore the design space and determine which set of designs best match the experimental data. This set of designs were then executed in NPHASE-CMFD and the results were added to the set of results obtained by the LHS step. This iterative process as described above and graphically depicted in Figure 2 was run until the additional NPHASE-CMFD runs no longer significantly increased the prediction accuracy of the RBF model.

#### 4. RESULTS

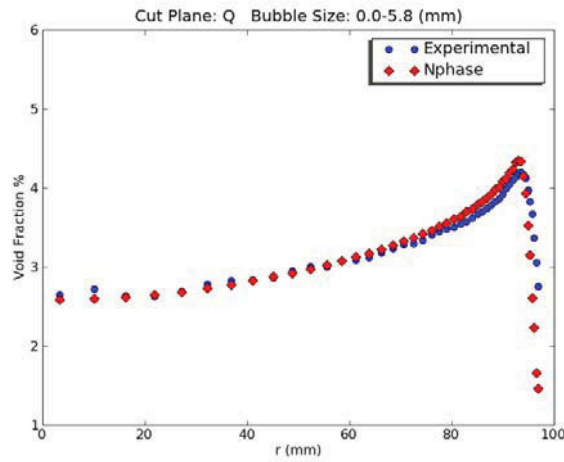
Computations were executed on the *icestorm* cluster, part of Idaho National Laboratory's high performance computing environment. Icestorm consists of a SGI Altix ICE 8200 distributed memory blade cluster comprised of 256 compute blades with two quad core Intel Xeon processors each. There are 2,048 compute cores total running at a clock speed of 2.66 GHz. The system has available 2 GB random access memory per core, offering 4 TB memory total and a 70 TB disk capacity. Users are connected via a DDR 4X InfiniBand interconnect network. The operating system is SUSE Linux Enterprise Server 10. The computational mesh was generated using Pointwise Gridgen Version 15.17, the CMFD simulations were run using NPHASE-CMFD Version 3.1.3 and the optimization studies were performed using Engineous iSIGHT-FD Version 3.1.

Computed profiles were compared to experimental data at a pipe length equal to 40 pipe diameters. Figures 3 through 6

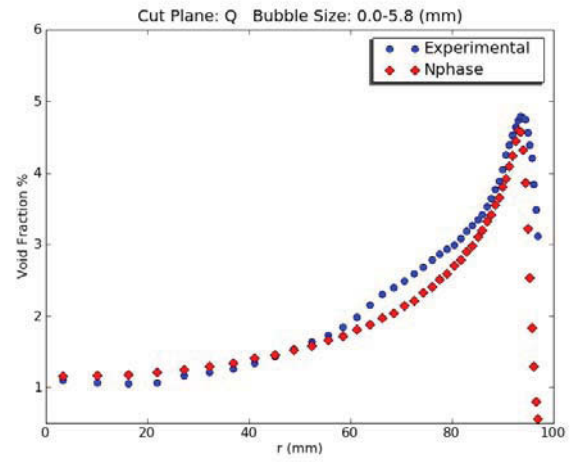
compare the radial distribution of void fraction for fields 2, 3, 4 and 5 predicted by the NPHASE-CMFD code to those obtained in the TOPFLOW experiments for Cases 118 and 140.

The void fraction of the smallest bubble size group (Field 2) is seen to peak a small distance away from the wall (Figure 3). This effect diminishes as bubble size increases (Figures 4 and 5). The measured radial void fraction distributions for the smaller bubbles show a characteristic peak near the wall. The small bubbles gravitate to the wall, whereas the large bubbles move towards the center of the pipe. The local peaking of the void fraction near the wall for the small bubbles is caused by the lift force that directs the small bubbles towards the wall interacting with the wall force that pushes the bubbles away from the wall. To numerically obtain radial void fraction distributions similar to those measured experimentally, it is necessary to specify a positive lift force coefficient for bubble groups 2, 3 and 4 and a negative lift force coefficient for bubble group 5. Note that if the water flow in the pipe was directed downwards, both the lift and wall forces for the small bubbles would be directed towards the center of the pipe and peaking of the void fraction would not occur near the wall [20].

In Figure 6 it is seen that the largest bubble group (Field 5 in the model) exhibits a Gaussian-shaped void fraction distribution with a maximum near the center of the pipe. For all cases, the void fraction approaches zero at the wall. The TOPFLOW data show an increase in void fraction (also called gas holdup) at higher gas injection flow rates. This effect has also been observed for air-water flow in bubble columns operating in the churn-turbulent regime[21].

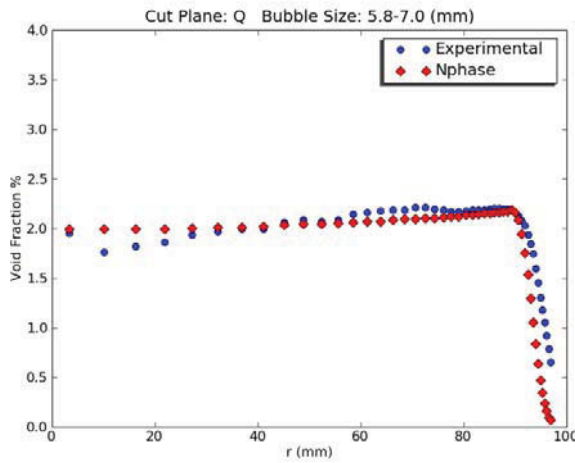


(a)

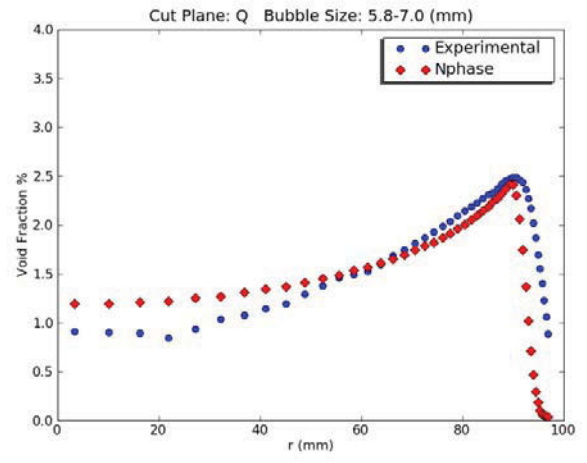


(b)

FIGURE 3. COMPARISON OF FIELD 2 COMPUTED VS. MEASURED RADIAL VOID FRACTION DISTRIBUTION FOR BUBBLES WITH DIAMETERS LESS THAN 5.8 MM (A) TOPFLOW CASE 118, (B) TOPFLOW CASE 140.

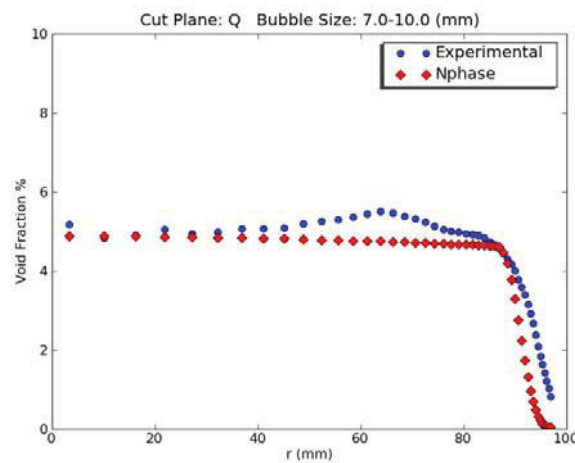


(a)

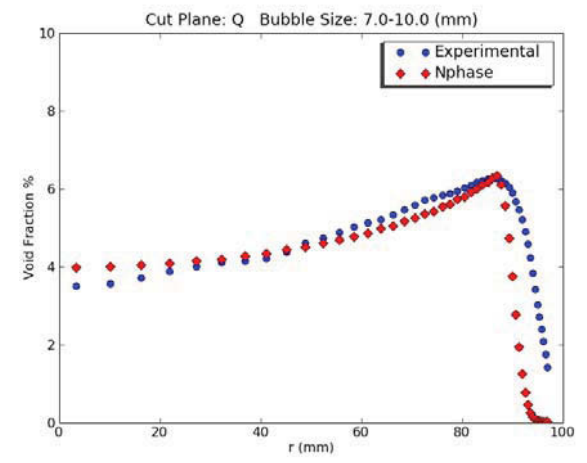


(b)

FIGURE 4. COMPARISON OF FIELD 3 COMPUTED VS. MEASURED RADIAL VOID FRACTION DISTRIBUTION FOR BUBBLES WITH DIAMETERS BETWEEN 5.8 MM AND 7.0 MM (A) TOPFLOW CASE 118, (B) TOPFLOW CASE 140.



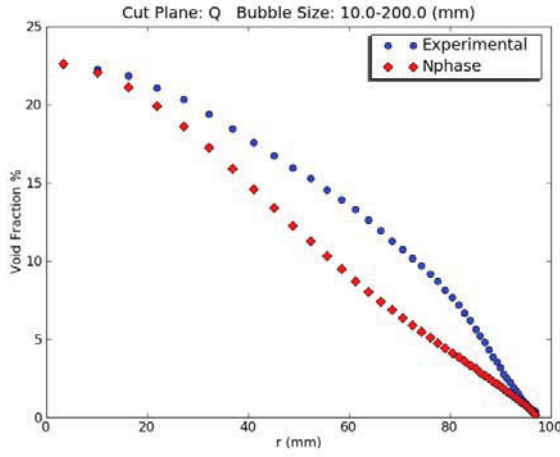
(a)



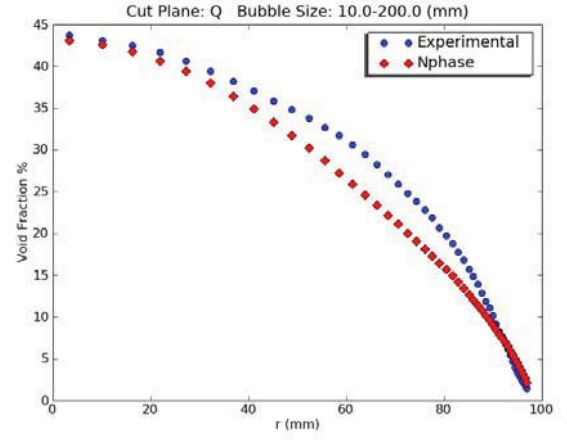
(b)

FIGURE 5. COMPARISON OF FIELD 4 COMPUTED VS. MEASURED RADIAL VOID FRACTION DISTRIBUTION FOR BUBBLES WITH DIAMETERS BETWEEN 7.0 MM AND 10.0 MM (A) TOPFLOW CASE 118, (B) TOPFLOW CASE 140.



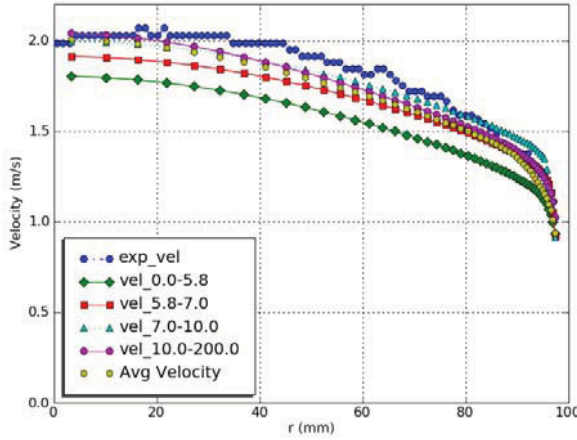


(a)

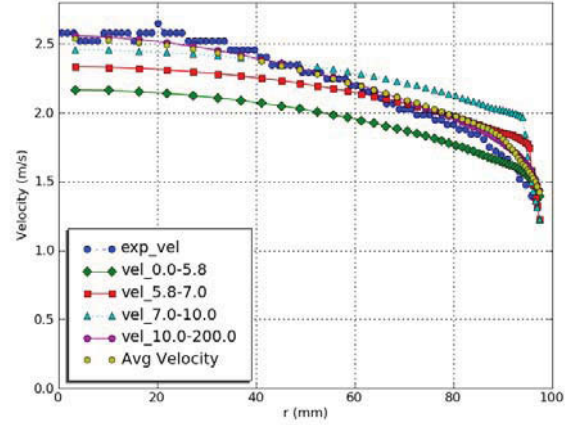


(b)

**FIGURE 6. COMPARISON OF FIELD 5 COMPUTED VS. MEASURED RADIAL VOID FRACTION DISTRIBUTION FOR BUBBLES WITH DIAMETERS GREATER THAN 10.0 MM (A) TOPFLOW CASE 118, (B) TOPFLOW CASE 140.**



(a)



(b)

**FIGURE 7. COMPARISON OF COMPUTED VS. MEASURED GAS VELOCITY RADIAL DISTRIBUTION (A) TOPFLOW CASE 118, (B) TOPFLOW CASE 140.**

Figure 7 compares the computed and measured nearly fully developed radial profile of gas velocity. The nearly fully developed average gas velocity is higher for Case 140 than Case 118, since the gas injection velocity is higher. The radial velocity distribution for all four bubble fields predicted by the model is shown along with an average velocity for all bubble fields. The experimental measurement shown is an average of all the bubble fields. The model predicts that the larger bubbles travel faster than the smaller bubbles. The large bubbles appear to be driving the flow, dragging the smaller bubbles along [22]. This occurs since the drag force increases with decreasing bubble size. The optimization process helps to define the necessary adjustment in drag coefficient by the correction factor for bubble ellipticity in Equation 7.

The Tomiyama correlation (Equation 17) provides a reasonable estimate for the lift force coefficient for bubble groups 2, 3 and 5. However, the correlation predicts a negative lift force coefficient for bubble group 4 (bubble diameters between 5.8 and 7.0 mm,) since the predicted critical spherical

bubble diameter is 5.8 mm. The TOPFLOW data shown in Figures 3 to 6 are based upon a sphere equivalent diameter. The data show a wall peak and a generally positive slope in the radial profile for bubble group 4. Several possible reasons for this discrepancy in critical bubble diameter are proposed. The correlation was obtained from experimental investigations on single bubbles in laminar flow in a water-glycerol solution. The TOPFLOW data were obtained for a turbulent air-water flow with a polydisperse bubble distribution. A continual process of bubble breakup and coalescence occurs in the flow due to a shearing of small bubbles from the larger bubbles and, at the same time, a coalescence of the smaller bubbles. This coalescence rate increases with the square of the bubble number density. Since the lift force moves the small bubbles to form a wall peak, the coalescence rate of the small bubbles is highest near the wall i.e. there is a source for bubbles of group 4 in the near wall region. If we assume, that the Tomiyama correlation is still valid for TOPFLOW conditions, these bubbles should migrate towards the pipe center, where

they coalesce to larger bubbles. That means that, even in case of a negative lift force coefficient for bubble group 4, a profile with a wall peak may be established due to the near wall source and the sink for this bubble group in the center. Another possible reason is bubble-bubble interaction. The large bubbles move upwards at a faster velocity than the small bubbles and this motion pushes the small bubbles away from the center of the pipe. It appears from the flattening radial void fraction profile of bubble group 4 for Case 118 that these competing processes are almost balanced. For the group 4 bubbles of Case 140, the radial void fraction profile is wall peaked. The higher gas flow rate causes higher shear forces that strip small bubbles from the larger ones. The larger momentum of these large bubbles pushes the small bubbles towards the wall and creates the wall peak shape of the radial void fraction profile. The transition from wall peaking to core peaking takes place at a lower critical bubble size for the lower superficial gas injection velocity. These dynamic processes currently are not represented in the simulations. For this reason a positive lift force coefficient has to be applied in the simulations for bubble group 4 to be consistent with the experimental observations.

Recommendations for improved CMFD simulations include incorporation of accurate bubble breakup and coalescence models. These results are limited to comparisons at nearly fully developed conditions. Future work will include mass transfer modeling and compare developing profiles for churn-turbulent flows.

## 5. SUMMARY

This work demonstrates the application of a design optimization process for the validation of CMFD results. Results obtained using an NPHASE-CMFD model for a five-field model of churn turbulent flow were compared with experimental data of adiabatic air-water flow in a vertical pipe taken at the Forschungszentrum Dresden-Rossendorf TOPFLOW facility. A five-field model was used to represent the poly-dispersed, two-phase flow. A commercial design optimization code (Engineous iSIGHT-FD) was applied to tune the interfacial force mechanistic models in the NPHASE-CMFD code. A set of coefficient terms to modify both the drag and non-drag interfacial forces was found that provide reasonable agreement with experimental data. This work demonstrates that the application of optimization software can be a valuable tool for CMFD validation to complement the application of best practices.

## ACKNOWLEDGMENTS

The experiments were carried out in the frame of a current research project funded by the German Federal Ministry of Economics and Labour, project number 150 1329. Funding for the computational work was supported by the U.S. Department of Energy, Office of Nuclear Energy, under DOE Idaho Operations Office Contract DE-AC07-05ID14517.

## Nomenclature

$A_{i,k}''$	$m^{-1}$	Interfacial area density
$A_k$	$m^2$	projected area
$C_D$		drag force coefficient
$C_L$		lift force coefficient
$C_{TD}$		turbulence dispersion force coefficient
$C_{VM}$		virtual mass force coefficient
$C_W$		wall force coefficient
$D_{h,k}$	$m$	maximum horizontal dimension of the bubble
$D_k$	$m$	bubble diameter
$E_o$		Eötvös number
$f$		shape factor for bubble eccentricity
$g$	$m/s^2$	gravitational acceleration
$k$	$kg/m^2 \cdot s^2$	effective turbulent kinetic energy of continuous field
$j_g$	$m/s$	superficial gas velocity
$j_l$	$m/s$	superficial liquid velocity
$\underline{M}$	$N/m^3$	Interfacial force per unit volume
$\underline{n}$		normal vector at wall
$r_{sm}$	$m$	Sauter mean radius
$r_d$	$m$	drag radius
$Re$		Reynolds number
$s$	$m$	distance between bubble and wall
$\underline{v}$	$m/s$	velocity
$\forall$	$m^3$	volume

## Superscripts

i	interfacial
D	drag
L	lift
ND	non-drag
TD	turbulent dispersion
VM	virtual mass
W	wall

## Subscripts

c	continuous phase
cr	critical
d	dispersed phase
k	field
m	mixture
sm	Sauter mean

## Symbols

$\alpha$	void fraction
$\mu$	$kg/m \cdot s$ viscosity
$\rho$	$kg/m^3$ density
$\sigma$	$N/m$ surface tension
$\tau$	$N/m^2$ shear stress
$\xi$	region of influence for wall force function

## REFERENCES

1. Antal, S.P., et al., *Development of a Next Generation Computer Code for the Prediction of Multicomponent Multiphase Flows*, in *International Meeting on Trends in Numerical and Physical Modeling for Industrial Multiphase Flow*. 2000: Cargese, France.
2. Lucas, D., Beyer, M., Kussin, J., Schutz, *Benchmark Database on the Evolution of Two-Phase Flows in a Vertical Pipe*, in *XCFD4NRS, OECD/NEA & International Atomic Energy Agency (IAEA) Workshop*. 2008: Grenoble, France.
3. Drew, D.A., Passman, S.L.. *Theory of Multicomponent Fluids*. Applied Mathematical Sciences, 1998. **Vol. 135**.
4. Sato, Y., Sekoguchi, K., *Liquid Velocity Distribution in Two-Phase Bubble Flow*. Int. J. Multiphase Flow, 1975. **Vol 2**: p. 79-95.
5. Sato, Y. and M. Sadatomi, *Momentum and Heat Transfer in Two-Phase Bubble Flow - I*. International Journal of Multiphase Flow, 1981. 7(2): p. 167-177.
6. Tselishcheva, E.A., Antal, S.P., Podowski, M.Z., Guillen, D.P., Beyer, M., Lucas, D. , *Development and Validation of a Multifield Model of Churn-Turbulent Gas/Liquid Flows*, in *Proceedings of the 17th International Conference on Nuclear Engineering, ICONE-17*. 2009, ASME: Brussels, Belgium.
7. Lopez de Bertodano, M., Sun, X., Ishii, M., Ulke, A., *Phase Distribution in the Cap Bubble Regime in a Duct*. Journal of Fluids Engineering, 2006. **Vol. 128**: p. p. 811-818.
8. Lucas, D., Krepper, E., Prasser, H.-M., *Prediction of Radial Gas Profiles in Vertical Pipe Flow on the Basis of Bubble Size Distribution*. Int. J. Therm. Sci., 2001. **Vol. 40**: p. p. 217-225.
9. Lucas, D., Krepper, E., Prassar, H.-M., *Use of Models for Lift, Wall and Turbulent Dispersion Forces Acting on Bubbles for Poly-Disperse Flows*. Chemical Engineering Science, 2007. **Vol. 62**: p. p. 4146-4157.
10. Podowski, M.Z., *On the Consistency of Mechanistic Multidimensional Modeling of Gas/Liquid Two-Phase Flows*. Nucl. Eng. Des. , 2009. **doi:10.1016/j.nucengdes.2008.10.022**.
11. Nedeltchev, S., *Simultaneous Application of Penetration Theory to Both Small and Large Bubbles Formed in a Column Operated Under Heterogeneous Regime*. Chem. Eng. Technol., 2008. **Vol. 31**(No. 2): p. p. 315-323.
12. Liu, Y., Hibiki, T., Sun, X., Ishii, M., Kelly, J.M., *Drag Coefficient in One-Dimensional Two-Group Two-Fluid Model*. International Journal of Heat and Fluid Flow, 2008. **Vol. 29**: p. p. 1402-1410.
13. Wallis, G.B., *One-Dimensional Two Phase Flow*. 1969, New York: McGraw-Hill.
14. Ishii, M., Zuber, N., *Drag Coefficient and Relative Velocity in Bubbly, Droplet or Particulate Flows*. AIChE Journal, 1979. **Vol. 25**: p. p. 843-855.
15. Clift, R., Grace, J.R., Weber, M.E., *Bubbles, Drops, and Particles*. 1978, Mineola, NY: Dover Publications, Inc.
16. Tomiyama, A., Tamai, H., Zun, I., Hosokawa, S., *Transverse Migration of Single Bubbles in Simple Shear Flows*. Chem. Eng. Sci., 2002. **Vol. 57**: p. p. 1849-1858.
17. Wellek, R.M., Agrawal, A.K., Skelland, A.H.P, *Shapes of Liquid Drops Moving in Liquid Media*. AIChE Journal, 1966. **Vol. 12**: p. p. 854-860.
18. Lucas, D., Krepper, E., Prasser, H.-M., Manera, A., *Investigations on the Stability of the Flow Characteristics in a Bubble Column*. Chem. Eng. Technol., 2006. **29**(9): p. p. 1066-1072.
19. Antal, S.P., M.Z. Podowski, R.T. Lahey, Jr., D. Barber, C. Delfino, *Multidimensional Modeling of Developing Two-Phase Flows in a Large Adiabatic Riser Channel*, in *The 11th International Topical Meeting on Nuclear Reactor Thermal-Hydraulic (NURETH-11)*. 2005: Popes Palace Conference Center, Avignon, France.
20. Antal, S.P., R.T. Lahey, Jr., Flaherty, J.E., *Analysis of Phase Distribution in Fully-Developed Laminar Bubbly Two-Phase Flow*. International Journal of Multiphase Flow, 1991. **Vol. 17**(Issue 5): p. p. 635-652.
21. Ong, B., *Experimental Investigation of Bubble Column Hydrodynamics - Effect of Elevated Pressure and Superficial Gas Velocity*, in *Department of Chemical Engineering*. 2003, Washington University: Saint Louis, Missouri.
22. Mudde, R.F., *Gravity-Driven Bubbly Flows*. Annual Rev. Fluid Mech., 2005. **Vol. 37**: p. p. 393-423.